CHAPTER 8

Combined Effect of Non-Darcian Flow and Semi-Permeable Drainage Boundaries on Unsaturated Consolidation

8.1 INTRODUCTION

The previous chapter explains the numerical approach for handling the one-dimensional consolidation of unsaturated clays, in detail. The focus of the previous chapter was to show the importance of non-uniform initial pore pressure distribution in the consolidation analysis of unsaturated soils. The other assumptions of the traditional unsaturated consolidation were retained in the previous chapter. In the present chapter, an attempt has been made to perform the unsaturated consolidation analysis by providing a relaxation on the drainage boundaries and the water flow laws. The importance and role of nonlinear flow and impeded boundary conditions are already discussed in Chapters 4 and 5.

Similar to Chapter 5, the top and bottom drainage boundaries are treated as impeded, which inhibits both air and water flow. The degrees of inhibition are chosen to differ for each boundary and fluid selected. By controlling the inhibition level, the top and bottom boundaries can transition between the two extreme drainage states: completely drained to completely undrained. Several researchers, including Zhou et al. (2017), Wang et al. (2017a, 2017b, 2018), and Moradi et al. (2019), proposed their theories regarding impeded boundary conditions in unsaturated clayey media. These studies were conducted based on the linear relationship between the fluid flow and the hydraulic gradient (Darcy's law). No such findings appear in the literature where unsaturated consolidation analyses are conducted based on the nonlinear v–i relationship. To invoke the nonlinear water flow,

Elnaggar et al.'s (1973) exponential and threshold gradient-based single equation is imposed, as was done in Chapter 4. By adjusting the exponent and the threshold gradient the flow can be reverted to Darcian flow.

This chapter aims to understand the consolidation of unsaturated soil enclosed by semi-permeable drainage boundaries and subjected to nonlinear water flow. A detailed 1-D consolidation analysis of the unsaturated clayey soil is performed by considering the drainage boundaries to be semi-permeable and the fluid flow to be non-Darcian. The transient flow in the vadose zone is formulated by using Fredlund and Rahardjo's (1993) linear partial differential equations. The combined effect of the semi-permeable drainage boundary and the non-Darcian flow are rigorously examined by plotting the isochrones and the consolidating curves. The impacts of the semi-impermeable drainage boundaries appear to be highly profound on the dissipation process of the pore water pressure. The excess pore air pressure dissipates much faster than the excess pore water pressure resulting in the two intervals of the consolidation curves related to the water phase. The settlement curves get appreciably influenced by the partial drainage boundary during the early stage of consolidation whereas, the flow nonlinearity impacts at the later stage of consolidation.

8.2 PROBLEM STATEMENT

A constant and uniform load of magnitude q is applied over a horizontal surface of a homogenous and unsaturated clayey layer having an infinite horizontal extent with thickness, h_s, and bounded by two semi-permeable drainage boundaries. The thicknesses of the hypothetical cushions impeding the drainage of the consolidating layer on the top and the bottom surfaces are, h_T and h_B, respectively. The permeabilities of the air phase and the water phase are denoted as k_{ai} and k_{wi}, respectively; here, the second subscript, i, indicates different layers, namely, soil layer (s), top impeded surface (T), and bottom impeded surface (B). Fig. 8.1 represents the schematic diagram of the problem.

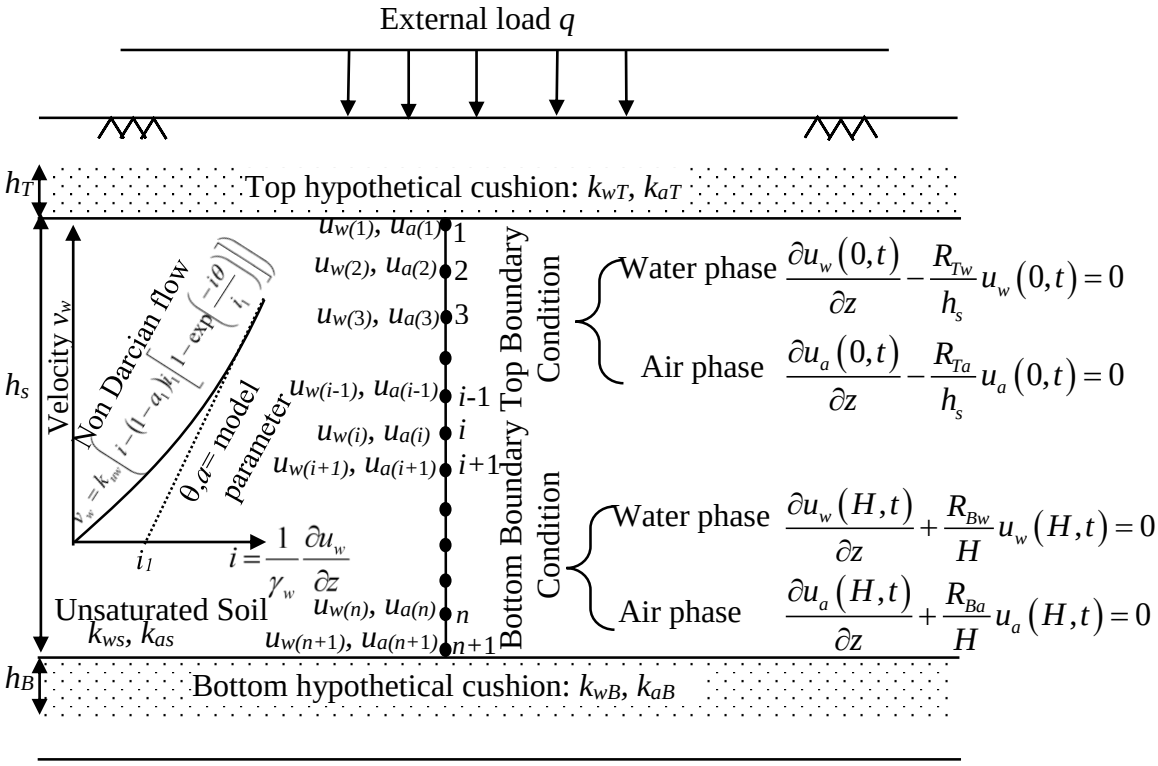

Fig. 8.1 Schematic representation of the chosen consolidating layer bounded by the semi-impermeable membranes.

With the advancement in time, the induced excess pore pressures get dissipated and return to the equilibrium state that existed prior to loading. The flow of water and air within the vadose zone is assumed to be governed by Elnaggar et al. (1973)'s non-linear law and Fick's (1855) linear law, respectively, were already discussed in Chapters 4 and 7, respectively.

The derivations of the one-dimensional uncoupled governing dissipation equations for water phase by assuming the flow of water phase governed by the Elnaggar et al. (1973)'s non-linear law detailed in Appendix F1. Air phase have the same equation as presented in Chapter 7. The problem statement including the boundary conditions (Moradi et al. 2019; Wang et al. 2017; Wang et al. 2017) can be written in the following canonical form:

Governing Differential Equations:

Water phase: $$\frac{\partial u_w}{\partial t} + C_w \frac{\partial u_a}{\partial t} = c_v^w \frac{\partial^2 u_w}{\partial z^2}\left(1-(1-a)\theta\left[1-\exp\left(\frac{-\theta}{i_1\gamma_w}\frac{\partial u}{\partial z}\right)\right]\right) \quad (8.1a)$$

Air phase: $$\frac{\partial u_a}{\partial t} + C_a \frac{\partial u_w}{\partial t} = c_v^a \frac{\partial^2 u_a}{\partial z^2} \quad (8.1b)$$

Subjected to:

i) Top Boundary Condition:

$$\text{Water phase: } \frac{\partial u_w(0,t)}{\partial z} - \frac{R_{Tw}}{h_s} u_w(0,t) = 0 \text{ ; where, } R_{Tw} = \frac{k_{wT} h_s}{k_{ws} h_T} \quad (8.2a)$$

$$\text{Air phase: } \frac{\partial u_a(0,t)}{\partial z} - \frac{R_{Ta}}{h_s} u_a(0,t) = 0 \text{ ; where, } R_{Ta} = \frac{k_{aT} h_s}{k_{as} h_T} \quad (8.2b)$$

ii) Bottom Boundary Condition:

$$\text{Water phase: } \frac{\partial u_w(h_s,t)}{\partial z} + \frac{R_{Bw}}{H} u_w(h_s,t) = 0 \text{ ; where, } R_{Bw} = \frac{k_{wB} h_s}{k_{ws} h_B} \quad (8.3a)$$

$$\text{Air phase: } \frac{\partial u_a(h_s,t)}{\partial z} + \frac{R_{Ba}}{H} u_a(h_s,t) = 0 \text{ ; where, } R_{Ba} = \frac{k_{aB} h_s}{k_{as} h_B} \quad (8.3b)$$

R_{Tw}, R_{Ta}, R_{Bw}, and R_{Ba} are the dimensionless non-negative semi-permeable parameters that reflect the efficiency of drainage at the respective boundaries. These four parameters are combinedly referred here as *R*-value. The fully pervious condition of a certain phase at a specific boundary is ascertained when the corresponding semi-permeable parameter approaches infinity; similarly, the drainage boundary becomes completely impervious if the corresponding *R*-value is enforced to be zero. Hence, the impeded boundary condition is regarded as a generalized form of the boundary condition; Dirichlet (pore pressures=0) and Neumann (pore pressure gradients=0) boundary conditions can be

retrieved by changing the drainage parameters. It is intended to verify the effect of non-Darcian flow on the consolidation behaviour of clayey stratum bounded by semi-permeable layers. The analysis is carried out in an uncoupled manner; this implies that during the evaluation of the excess pore-water and pore-air pressures dissipation, the stress-deformation process is not encountered in the analysis.

8.3 NUMERICAL ANALYSIS

The parabolic *partial differential equations* (PDEs), as presented in Eqs. 8.1a and 8.1b, are rearranged to obtain the following relationship of the time derivative of a certain phase in terms of the space derivative of other phases.

$$\frac{\partial u_w}{\partial t} = \frac{1}{1-C_a C_w}\left(c_v^w \frac{\partial^2 u_w}{\partial z^2}\left(1-(1-a)\theta\left[1-\exp\left(\frac{-\theta}{i_1\gamma_w}\frac{\partial u}{\partial z}\right)\right]\right) - C_w c_v^a \frac{\partial^2 u_a}{\partial z^2}\right) \tag{8.4a}$$

$$\frac{\partial u_a}{\partial t} = \frac{1}{1-C_a C_w}\left(c_v^a \frac{\partial^2 u_a}{\partial z^2} - C_a c_v^w \frac{\partial^2 u_w}{\partial z^2}\right) \tag{8.4b}$$

The consolidating layer is discretized with (n+1) number of equally spaced grid points, as shown in Fig.8.1. For obtaining the spatial and temporal variation of u_w and u_a, Eqs. (8.5a) and (8.5b) are to be solved simultaneously at each grid point. Considering the complexity of the analytical procedure, simulations are carried out by employing the Crank-Nicolson (CN) semi-implicit scheme of finite difference numerical technique. According to the CN scheme, the PDEs at any arbitrary grid point (GP), i, can be expressed as

$$\left.\frac{\partial u_w}{\partial t}\right|_{@\, i^{th}GP} = \frac{1}{1-C_a C_w}\left(c_v^w \left.\frac{\partial^2 u_w}{\partial z^2}\right|_i \underbrace{\left(1-(1-a)\theta\left[1-\exp\left(\frac{-\theta}{i_1\gamma_w}\left.\frac{\partial u_w}{\partial z}\right|_i^t\right)\right]\right)}_{E_i^t} - C_w c_v^a \left.\frac{\partial^2 u_a}{\partial z^2}\right|_i\right) \tag{8.5a}$$

$$\left.\frac{\partial u_a}{\partial t}\right|_{@i^{th}GP} = \frac{0.5}{1-C_aC_w}\left(c_v^a\left(\left.\frac{\partial^2 u_a}{\partial z^2}\right|_i^{t+\Delta t} + \left.\frac{\partial^2 u_a}{\partial z^2}\right|_i^{t}\right) - C_a c_v^w\left(\left.\frac{\partial^2 u_w}{\partial z^2}\right|_i^{t+\Delta t} + \left.\frac{\partial^2 u_w}{\partial z^2}\right|_i^{t}\right)\right) \quad (8.5b)$$

To remove the non-linearity in Eq. (8.6a), the space gradient of u_w in the exponent term is evaluated at the previous (known) time-step. Each internal GPs must satisfy the governing differential equations and the extreme GPs are required to satisfy the following constraints:

For top boundary:

Water Flow Boundary	Air Flow Boundary
$\left.\frac{\partial u_w}{\partial z}\right\|_{z=0} - \frac{R_{Tw}}{h_s}u_w\|_{z=0} = 0$	$\left.\frac{\partial u_a}{\partial z}\right\|_{z=0} - \frac{R_{Ta}}{h_s}u_a\|_{z=0} = 0$
$\frac{u_{w(2)}^{t+\Delta t} - u_{w(0)}^{t+\Delta t}}{2\Delta z} - \frac{R_{Tw}}{h_s}u_{w(1)}^{t+\Delta t} = 0$	$\frac{u_{a(2)}^{t+\Delta t} - u_{a(0)}^{t+\Delta t}}{2\Delta z} - \frac{R_{Ta}}{h_s}u_{a(1)}^{t+\Delta t} = 0$
$u_{w(0)}^{t+\Delta t} = u_{w(2)}^{t+\Delta t} - \frac{2R_{Tw}\Delta z}{h_s}u_{w(1)}^{t+\Delta t}$	$u_{a(0)}^{t+\Delta t} = u_{a(2)}^{t+\Delta t} - \frac{2R_{Tw}\Delta z}{h_s}u_{a(1)}^{t+\Delta t}$

(8.6a)

For bottom boundary:

$\left.\frac{\partial u_w}{\partial z}\right\|_{z=h_s} + \frac{R_{Bw}}{h_s}u_w\|_{z=h_s} = 0$	$\left.\frac{\partial u_a}{\partial z}\right\|_{z=h_s} + \frac{R_{Ba}}{h_s}u_a\|_{z=h_s} = 0$
$\frac{u_{w(n+2)}^{t+\Delta t} - u_{w(n)}^{t+\Delta t}}{2\Delta z} + \frac{R_{Bw}}{h_s}u_{w(n+1)}^{t+\Delta t} = 0$	$\frac{u_{a(n+2)}^{t+\Delta t} - u_{a(n)}^{t+\Delta t}}{2\Delta z} + \frac{R_{Ba}}{h_s}u_{a(n+1)}^{t+\Delta t} = 0$
$u_{w(n+2)}^{t+\Delta t} = u_{w(n)}^{t+\Delta t} - \frac{2R_{Bw}\Delta z}{h_s}u_{w(n+1)}^{t+\Delta t}$	$u_{a(n+2)}^{t+\Delta t} = u_{a(n)}^{t+\Delta t} - \frac{2R_{Ba}\Delta z}{h_s}u_{a(n+1)}^{t+\Delta t}$

(8.6b)

Thus, CN scheme converts the PDEs into simultaneous set of linear algebraic equations. The formation of the algebraic equations for each node and the resulting coefficient matrix are detailed in Appendix F2. The coefficient matrix, *G*, contains four non-dimensional terms, $\lambda_{1(i)}^t$, λ_2, λ_3, and λ_4 for any arbitrary GP, *i*; $\lambda_{1(i)}^t$, and λ_2 are related with the water phase, and λ_3, and λ_4 are associated with the air phase. It is also noteworthy that $\lambda_{1(i)}^t$ is the only space- and time- dependent variable term; rest of the terms are constant. The entire numerical simulations are performed by developing a suitable code in *MATLAB* (version R2018a). Here, Δz and Δt represents the user-defined depth and the

time increment, respectively. In the present analysis, 100 segments (n) are chosen. Thus, Δz becomes 0.1m. Further, Δt is taken to be 100 sec. The increments are chosen based on the fact that any further refinement will not make any difference in the computed solutions.

8.4 RESULT AND DISCUSSION

8.4.1 Dissipation of u_{w0} and u_{a0}

This section presents the variation of computed field variables (u_w and u_a) with the advancement in consolidation process by disseminating the local and global information in three different forms: normalized isochrones, average degree of consolidation (also known as representative settlement curves), and degree of consolidation at various specific points. The isochrones are normalized with respect to the initial excess pore pressures of the corresponding phases. For the chosen input parameters (q=100 kPa, n=0.5, S=0.80, $k_{ws}=10^{-10}$ m/sec, $m_{1k}^{s} = -2.5\times10^{-4}$ kPa, $m_2^s / m_{1k}^s = 0.4$, $m_{1k}^w / m_{1k}^s = 0.2$, and $m_{1k}^w / m_2^w = 0.25$), the magnitude of u_{w0} and u_{a0} are 38.88 and 18.55 kPa, respectively.

Figs. 8.2 and 8.3 present the variation of normalized u_w and u_a isochrones corresponding to different time, drainage conditions, material, and non-Darcian parameters. Fig. 8.2 depicts the variation of pore pressure isochrones at different time pertaining to (i) two different asymmetric drainage boundary conditions (R_T=200, R_B= 10; R_T=20, R_B=5), and (ii) different air-water permeability ratios (k_{ws}/k_{as}=0.1, 1 and 10); Figs. 8.2(a-c) show the isochrones after a relatively short span of consolidation (at $t=2.5\times10^6$ sec) and Figs. 8.2(d-f) present the isochrones after the passage of a large amount of time ($>10^8$ sec). The isochrones are evidently asymmetric and take the form of an inverted bowl shape with vertically aligned foot-surface. The base surface which remains flat in the initial stage of consolidation turns to be curved surface at a relatively larger time. The spread of the bowl foot expands for lower values of k_{ws}/k_{as}. Notably, at the drainage surfaces, the

isochrones are neither having a zero-pore pressure value (as in Dirichlet's criterion) nor orthogonality condition (as in Neumann criterion). In Figs. 8.2(d-f), there is no trace of the existence of excess PAP in the entire domain. Due to its small viscosity, the excess PAP dissipates much faster than the excess PWP. Although, the *R*-values impact the dissipation process of both the phases (air and water) nevertheless, the overall influence of the impeded boundary conditions are highly profound on the water phase in comparison to the air phase. The higher the values of *R*, the corresponding boundary surface becomes more drainable, and eventually, the lateral spread of the isochrones at that boundary surface becomes smaller. From Figs. 8.2(a-c), it is observed that the change in the *R*-values manifests the maximum deviation in the u_w-isochrones near the drainage surfaces, whereas, the u_a-isochrones vary significantly adjacent to the mid-section of the soil layer. The *R*-value induced isochrone-gap, termed here as r_{ig}, increases as the consolidation process advances. During the initial phase of consolidation, the r_{ig} remains to be greater near the drainage surfaces and quite smaller at the mid-portion. After a sufficient passage of time, the value of r_{ig} at the mid-section commensurate with its boundary zones. The air-water permeability ratio (k_{ws}/k_{as}) of the unsaturated consolidating layer also impacts the magnitude of r_{ig} appreciably. The magnitude of r_{ig}, especially at the mid-section, increases with the increase in k_{ws}/k_{as} ratio. For an instance, when k_{ws}/k_{as} equals to 1, the isochrones generated from different *R*-values get separated and becomes almost distinct at a relatively lower time (t =8.2x10^7 sec) whereas, for lower permeability ratio (k_{ws}/k_{as} =0.01) the corresponding isochrones remain inseparable (i.e., $r_{ig}\approx 0$) for a large portion near the mid-section even at a later stage of consolidation (t =2.3x10^9 sec). Fig. 8.2 also displays the effect of non-Darcian flow on the isochrones pertaining to the semi-permeable drainage surfaces; the chosen non-Darcian model parameters are: a=0.2, θ=0.5, and i_1=45. The deviation between the Darcian flow induced-curve (DF) and the non-Darcian flow induced-curve (NDF)

enlarges with the passage of consolidation time and with the increase in k_{ws}/k_{as} ratio. The variation between the Darcian and non-Darcian curves are quite prominent for k_{ws}/k_{as}=10. This figure gives a clear impression that the deviations between DF and NDF curves initially generates at the lateral sides adjacent to the base of the inverted bowl-shaped isochrones. With the progress in consolidation process, the base of the isochrones become curvilinear and the flow law induced isochrone gap, termed here as f_{ig}, becomes wider, especially visible in the mid-portion of the compressible stratum.

Fig. 8.3 illustrates the effect of non-Darcian fluid parameters. Corresponding to k_{ws}/k_{as} =0.1, different combinations of a- (=0.2, 0.5, and 0.8), θ- (=0.1, 0.5, and 1), and i_1 parameters (=5, and 45) are chosen with respect to double-drainage layer (R_T=R_B=∞), and semi-impermeable membrane (R_T=R_B=10). The isochrones are plotted at two different times, namely, t_1 =2.1×10^8 sec and t_2 =2.2×10^9 sec. The higher the flow nonlinearity (i.e., lower value of a and/or higher value of θ), the slower is the consolidation process. The θ-parameter appears to be more impactful than the a-parameter. However, the variation in i_1 hardly have any visual impact on the plotted u_w-isochrones. Irrespective of the R-value, f_{ig} remains maximum near the drainage surface for a considerable period of dissipation (even at t=t_1). At later stage (e.g. at t=t_2) the maximum f_{ig} shifts towards the middle portion of the consolidating layer. As the R-value of a surface becomes lesser and lesser (i.e. approaching towards Neumann's undrained boundary condition), the f_{ig} corresponding to that surface grows in size.

Fig. 8.4 presents the normalized NDF and DF isochrones by varying the thickness of the consolidating layer (h_s=1m, 5m, 10m and 50m); Fig. 8.4(a) corresponds to the same time (T=3.5×10^6 sec) and Fig. 8.4(b) represent the isochrones for the same time factor (T_{vw}=0.02). The R-parameters are kept same (R_T=R_B=10) indicating that the thicknesses of the hypothetical layers (i.e. h_T and h_B) gets changed accordingly. The chosen non-Darcian

model parameters are: a=0.2, i_1=5 and θ=0.5. Evidently, the consolidation for the shallow clay layer happens to be faster and therefore, for the chosen time-period [Fig. 8.4(a)], the area encompassed by the isochrone corresponding to h_s=1m is significantly less in comparison to the isochrone generated from h_s=50m.

At the chosen time period, the non-linear flow law is unable to make an impact on the consolidation process for the relatively thicker clay layer; however, for h_s=1m, the magnitude of f_{ig} is appreciably higher. Regardless of R_T/h_s and R_B/h_s, the isochrones corresponding to a specific T_{vw} coalesces to a single curve; however, the time required to attain the chosen time factor is noticeably different for the different layers. It can be interpreted that as the thickness increases the impeded boundary condition shifted towards the Neumann drainage boundaries condition and the difference between NDF and DF also decreases.

Fig. 8.5 outline the form of normalized isochrones for three different values of R_B (=1, 5, and 10) corresponding to two different drainage surfaces at the top, namely, fully drained ($R_T=\infty$) and fully undrained ($R_T=0$). Irrespective of the drainage condition on the top surface, the deviations of the isochrones due to the variation in R_B-values are reflected near the bottom drainage surface only. However, the r_{ig} value recorded at the bottom surface between $R_B=1$ and $R_B=5$ is quite higher than the r_{ig} value recorded between $R_B=5$ and $R_B=10$. The variations in the Darcian and non-Darcian flow (i.e. the existence of the non-zero f_{ig}) is visible for the entire layer if the top surface is of drained type but, the undrained top surface confines the impact of flow law adjacent to the bottom surface only. Quantitatively, the value of f_{ig} is appreciably higher if the top surface is of drained type. For drained top surface, f_{ig} increases continuously upto a certain depth (say, z/h_s=0.4-0.5) and attains a maximum value, thereafter, f_{ig} starts decreasing.

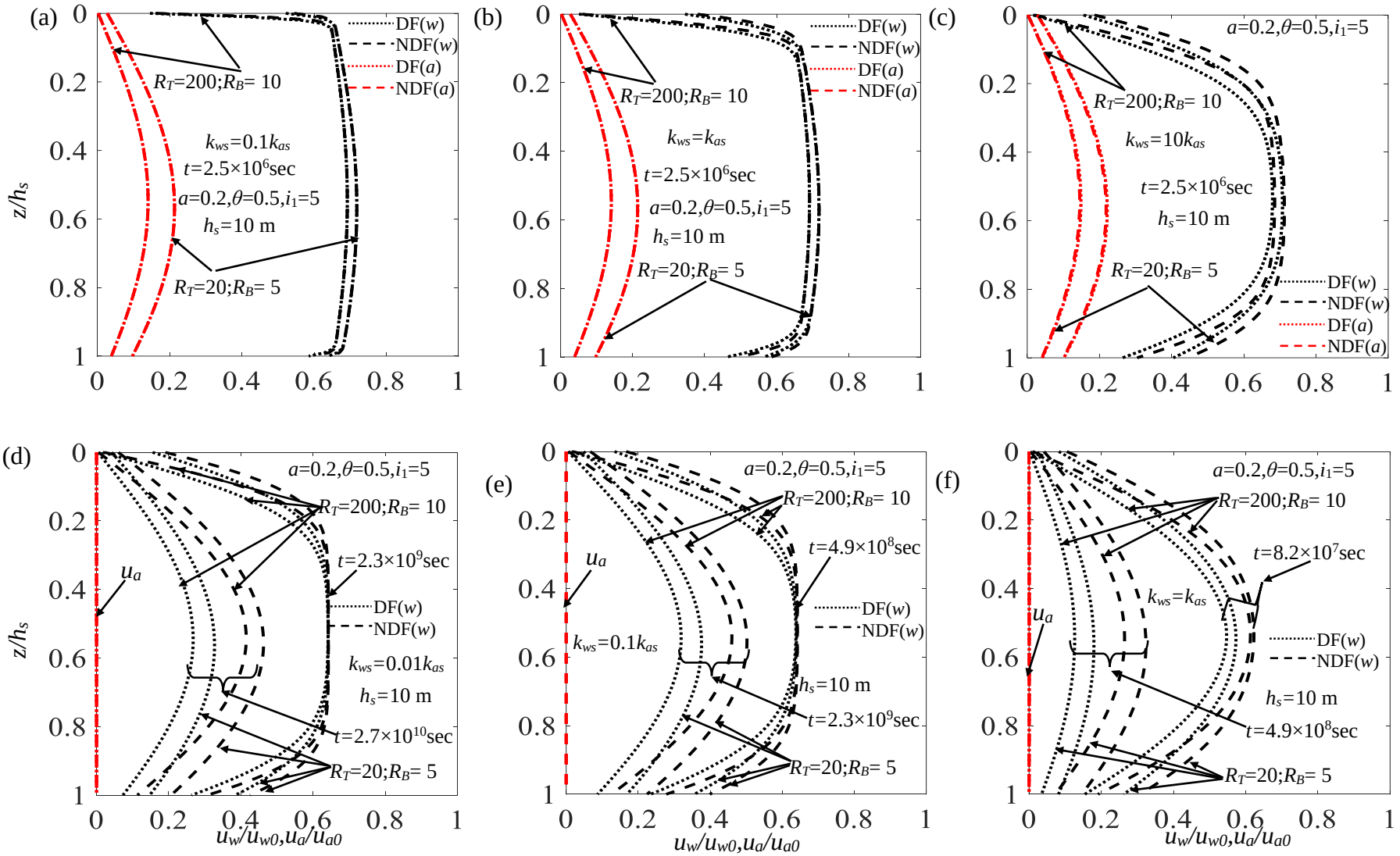

Fig. 8.2 The normalized pore pressure isochrones (Darcian and non-Darcian) with two asymmetric semi-permeable boundaries (R_T=200, R_B=10 and R_T=20, R_B=5) corresponding to relatively (a-c) early stage of consolidation (t=2.5×10^{6}sec) with k_{ws}/k_{as} equals to: (a) 0.1, (b) 1, (c) 10, and (d-f) later stage of consolidation ($t \gtrapprox 10^8$sec) with k_{ws}/k_{as} equals to: (d) 0.01, (e) 0.1, and (f) 1.

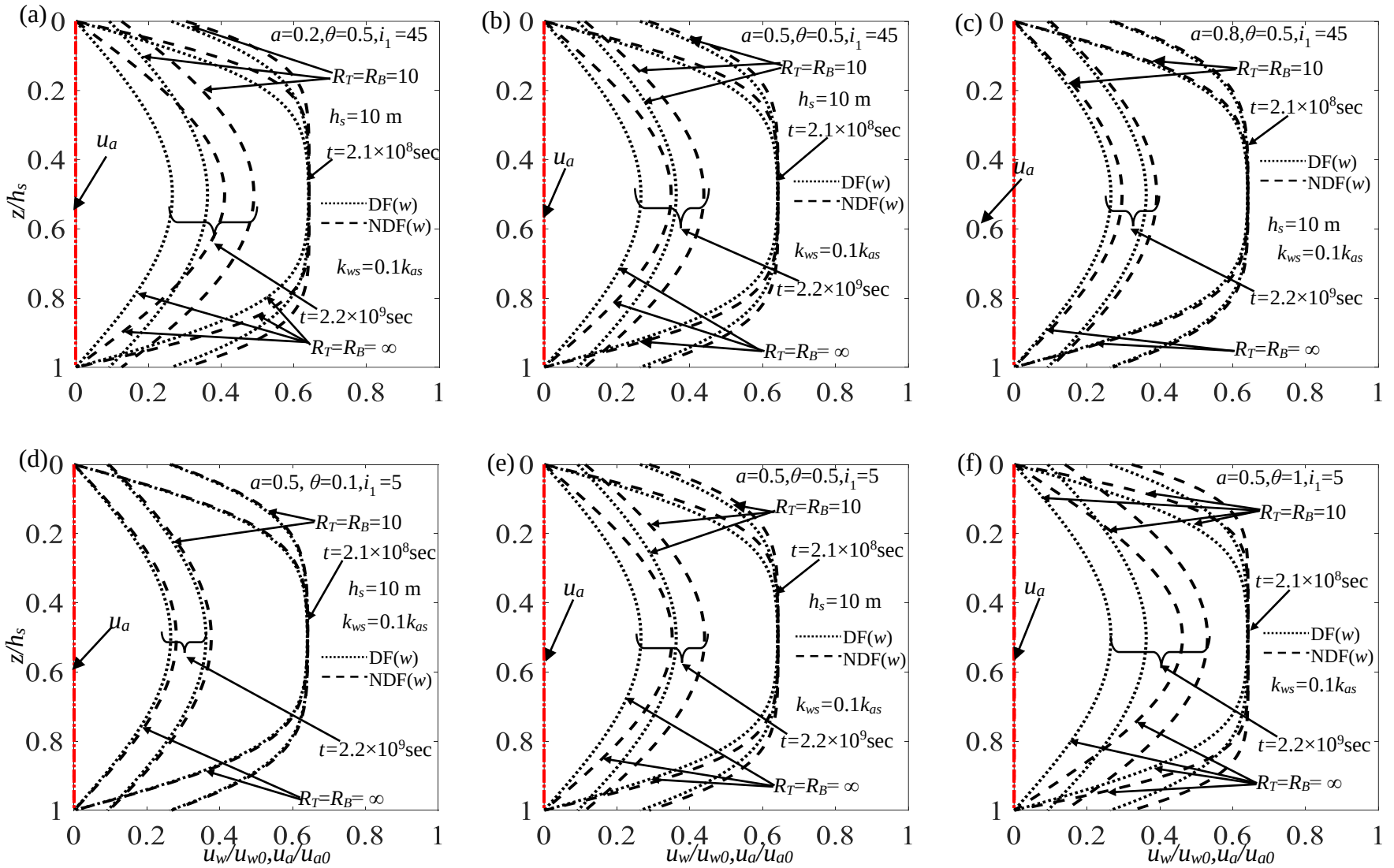

Fig. 8.3 The normalized pore pressure isochrones (Darcian and non-Darcian) having boundrirs parameters R_T=R_B=10 and R_T=R_B=∞ at two different times (t=2.1×10^{8}sec and t=2.2×10^{9}sec) corresponding to different non-Darcian flow parameters: (a) a=0.2,θ=0.5,i_1=45; (b) a=0.5,θ=0.5,i_1 =45; (c) a=0.8,θ=0.5,i_1=45; (d) a=0.5,θ=1,i_1=5; (e) a=0.5,θ=0.5,i_1=5; and (f) a=0.5,θ=1,i_1 =5.

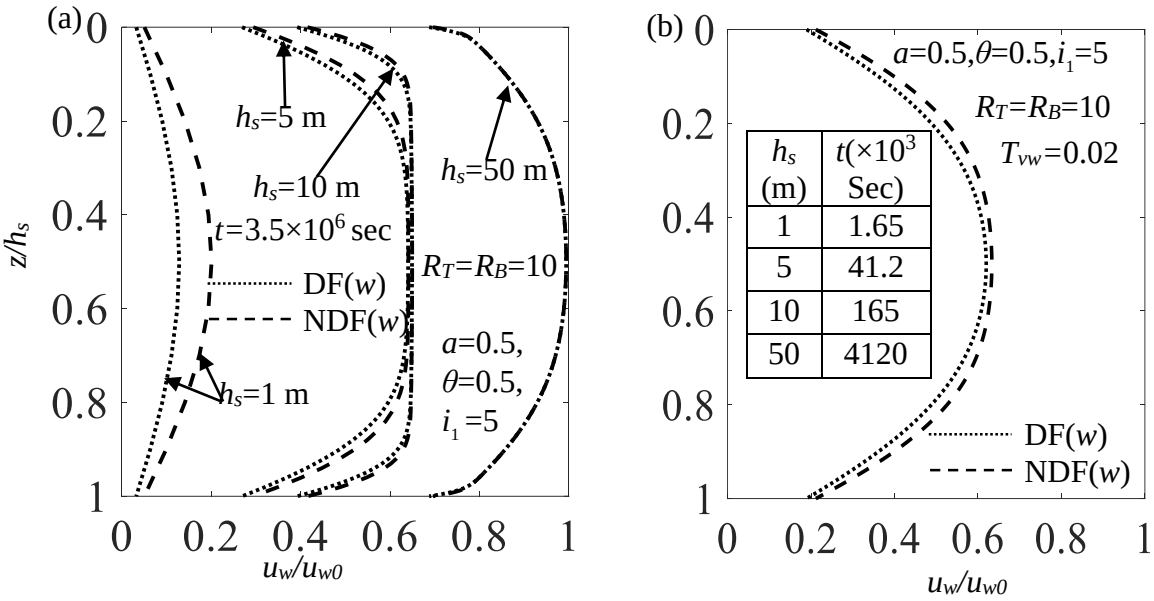

Fig. 8.4 The variation of normalized pore water pressure isochrones (Darcian and non-Darcian) corresponding to four different layer thicknesses (h_s=1m,5m,10m, and 50m) with R_T=R_B=10 and reported at the same (a) time (t=3.5×10^6 sec) and (b) time-factor (T_{vw}=0.02)

Figs. 8.6-8.8 present the variations of $U_{avg,w}$ and $U_{avg,a}$ with respect to the consolidation time; in Figs. 8.6-8.8 the R-value chosen at any boundary surface are the same for both the fluid phases, Fig. 8.6 displays the consolidating curves for three different drainage layers: (a) single (top) drainage (R_T =∞ and R_B =0) layer (SDL), (b) semi-permeable (R_T =10 and R_B =10) layer (SPL), and (c) double drainage (R_T =∞ and R_B =∞) layer (DDL). The curves are plotted for k_{ws}=k_{as} and corresponding to various non-Darcian parameters (a, θ, i_1). The consolidating curves for both the phases (air and water) are quite distinct and the curves associated with the chosen SPL always lie between the curves generated from the SDL and DDL; the SDL and DDL curves manifest the slowest and fastest rate of consolidation. The $U_{avg,a}$ curves are continuous whereas, the $U_{avg,w}$ curves show two intervals of the excess PWP dissipation- the first interval subscribe to the existence of the excess PAP and the second interval emerges after the complete dissipation of the excess PAP. A horizontal plateau exists between these two intervals. The discrepancy

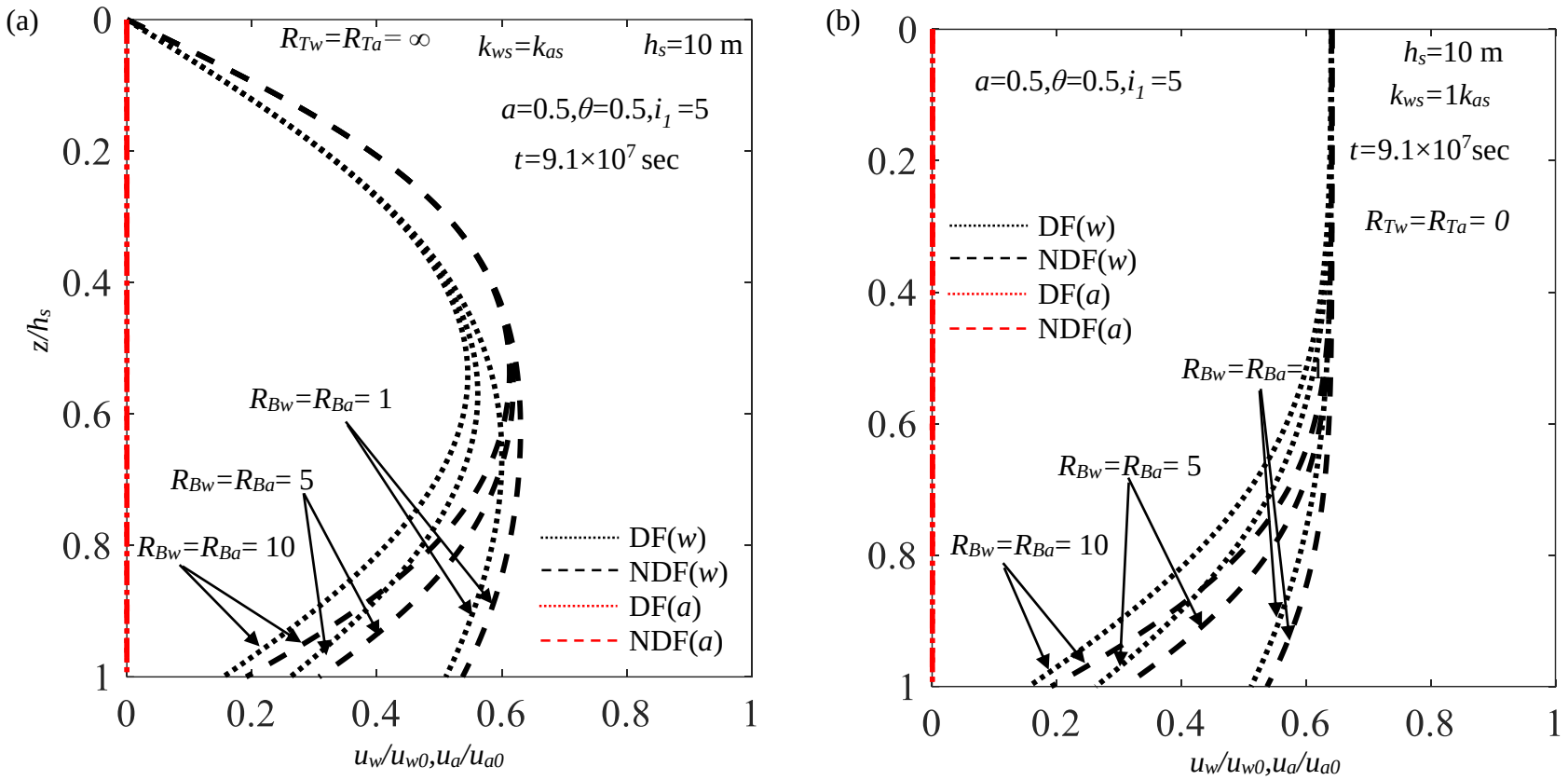

Fig. 8.5 The variation of normalized pore water pressure isochrones (Darcian and non-Darcian) at t=9.1×10^{7}sec with three different bottom conditions (namely, R_B=1, 5, and 10) and two different level of permeability at the top surface: (a) $R_{Tw}=R_{Ta}=\infty$ and (ii) $R_{Tw}=R_{Ta}=0$.

in the $U_{avg,w}$ curves due to the flow nonlinearity emerges after the complete dissipation of excess PAP.

This deviation gets wider with the advancement in time, and increment in flow nonlinearity (i.e. lower a and/or higher θ); nevertheless, the gap between the $U_{avg,w}$ curves due to the various flow law seems to be unaffected by the drainage boundary conditions. It can be interpreted that the settlement curve gets appreciably influenced by the partial drainage boundary from the early stage of consolidation whereas, the effect of flow nonlinearity gets visibly observed at the later stage of consolidation.

Fig. 8.7 displays the consolidating curves for three different symmetric SPLs (R_T =R_B= 1, R_T =R_B= 5, and R_T =R_B=100) subjected to Darcian and non-Darcian (a=0.2, θ=0.5, and i_1 =5) flows and corresponding to different permeability ratios, namely, k_{ws}/k_{as} equal to 0.01, 0.1, and 1. Irrespective of the k_{ws}/k_{as}, the curves generated from R_T =R_B= 5 lie between the curves pertaining to R_T =R_B=1 and R_T =R_B=100. The higher the permeability ratio, the faster the dissipation of u_w. The extent of the horizontal plateau between the two intervals of $U_{avg,w}$ curves prolongs for a longer period corresponding to a lower value of k_{ws}/k_{as}. The $U_{avg,w}$ curves representing different R-values are more distinct for higher k_{ws}/k_{as}. Moreover, higher permeability ratio also manifests the impacts of the flow law on the consolidation curves at a very early stage of consolidation.

Fig. 8.8 displays the consolidating curves for three different asymmetric SPLs: completely drained [Fig. 8.8(a)] and completely undrained [Fig. 8.8(b)] top surface with three semi-permeable bottom surfaces (R_B =1, 10, and 100). The distinctness of the $U_{avg,w}$ curves due to the variation in R_B values become more prominent when the top surface is considered to be completely impermeable (R_T=0). This can be attributed to the fact that the gap between the $U_{avg,a}$ curves corresponding to R_B =1 and R_B =10 are notably higher when

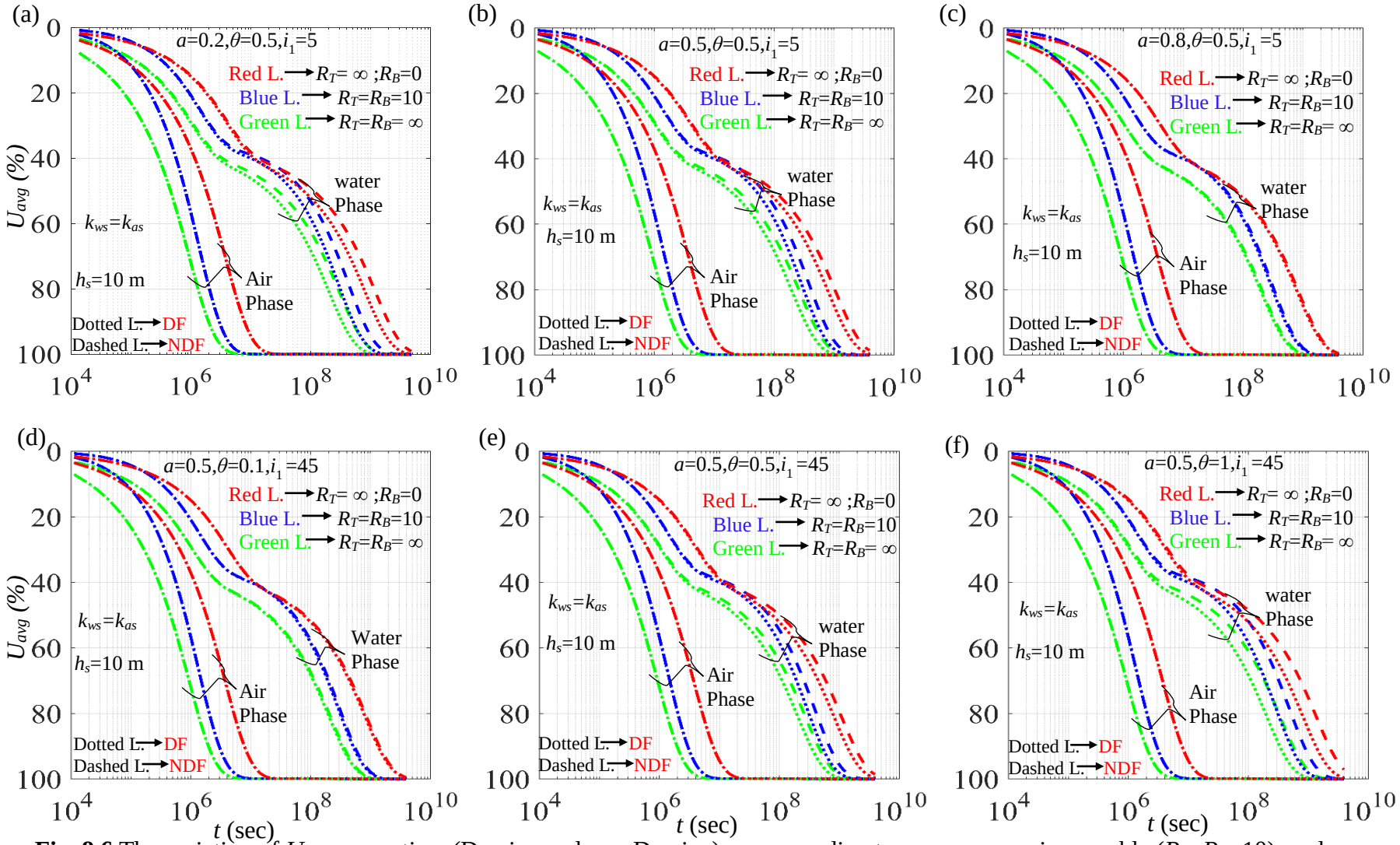

Fig. 8.6 The variation of U_{avg} versus time (Darcian and non-Darcian) corresponding to one-way, semipermeable (R_T=R_B=10), and two-way drainage systems by varying the non-Darcian flow parameters: (a) a=0.2, θ=0.5,i_1=5; (b) a=0.5,θ=0.5,i_1=5; (c) a=0.8,θ=0.5,i_1=5; (d) a=0.5,θ=1, i_1=45; (e) a=0.5,θ=0.5, i_1=45; and (f) a=0.5,θ=1, i_1=45.

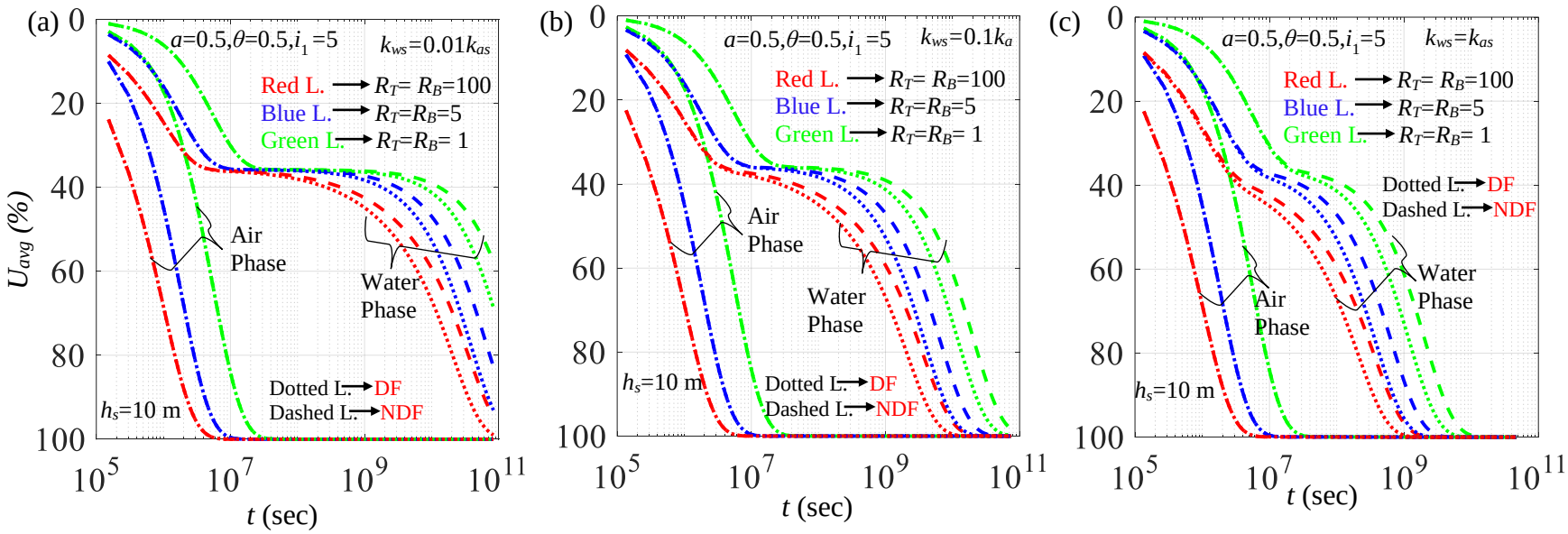

Fig. 8.7 The variation of U_{avg} versus time (Darcian and non-Darcian) corresponding to three different semipermeable (R_T (=R_B) =1, 5, or 10) drainage systems with a=0.2, θ=0.5, i_1=5 and permeability ratios (k_{ws}=0.01k_{as}) equals to (i) 0.01. (ii)0.1, and (1).

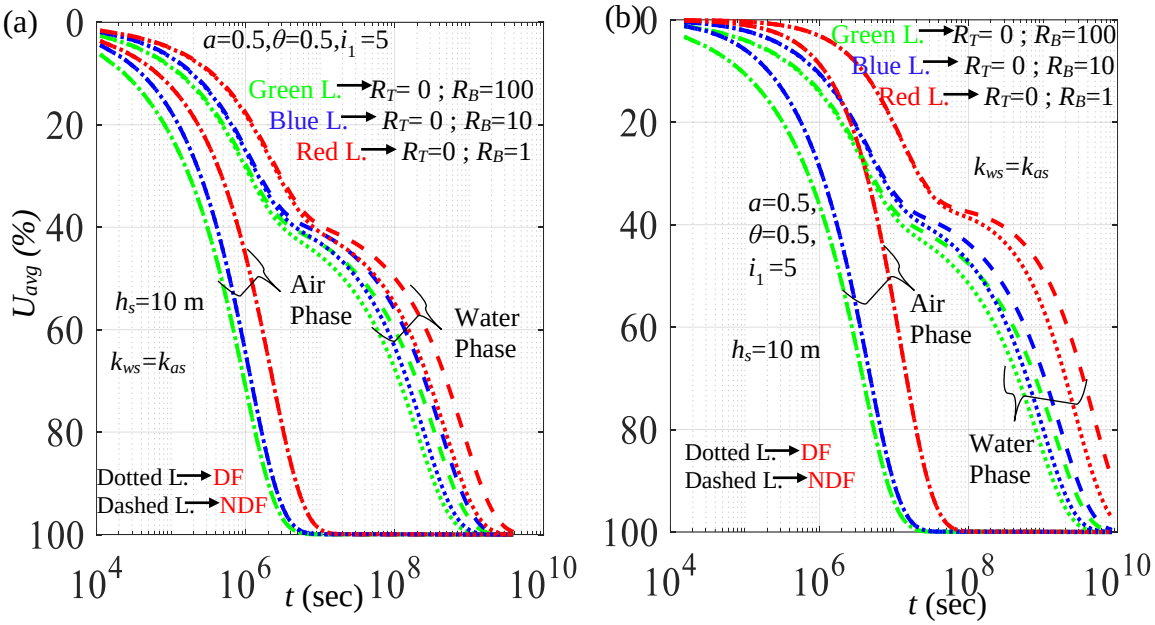

Fig. 8.8 The variation of U_{avg} versus time (Darcian and non-Darcian) for different semi-permeable bottom layer (R_B=1, 10, and 100), with a=0.2, θ=0.5, i_{tg}=5, k_{ws}=k_{as} and different drainage condition at the top: (a) fully pervious (R_T=∞), and (b) completely impervious (R_T=0).

R_T=0. The deviation between Darcian and non-Darcian curves also increases when the top surface is completely impermeable.

The consolidating curves impress upon the fact that up to a certain percentage of consolidation, Darcian and non-Darcian flow do not show any differences in the consolidating curves. After a specific time (t_{sp}), the gap between these two curves widens up. Fig. 8.9 shows the variation of t_{sp} profiles with respect to R_{Tw} and R_{Ta}; the flow ability of the fluid phases across the bottom surface is consider to be the same (R_{Bw}=R_{Ba}=10 / R_{Bw}=R_{Ba}=10000) in Fig. 8.9(a), and different (R_{Bw}=100, R_{Ba}=1 / R_{Bw}=10, R_{Ba}=50) in Fig. 8.9(b). In Fig. 8.9(a), while investigating the influence of R_{Ta} (or R_{Tw}) the top surface is resilient towards the water flow (or air flow). With an increase in R_{Tw}, t_{sp} decreases (up to the order of 2); conversely, the higher the R_{Ta}, the higher the t_{sp}. It can be interpreted that the influence of flow law become more prominent and rapid as the drainage surface

becomes more pervious to water flow but less pervious to air flow. The *R*-values at the bottom surface manifests the same observations. The change of R_B from 10 (i.e. close to undrained condition) to 10000 (i.e. close to drained condition) results in lowering of the t_{sp} values. The lower R_{Bw} and higher R_{Ba} values push the R_{Tw} -variant t_{sp} profiles to the higher side.

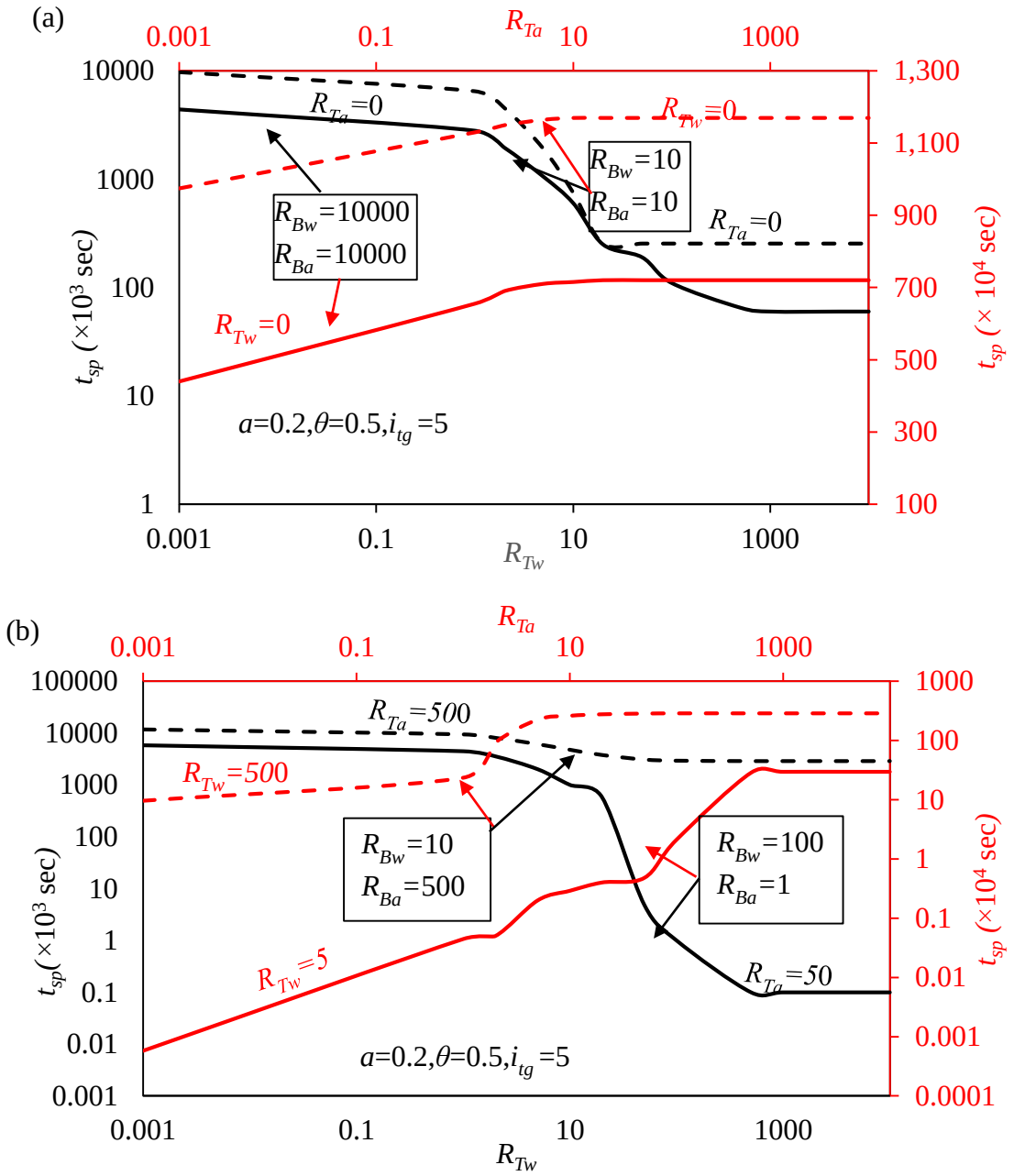

Fig. 8.9 The variation of t_{sp} with R_{Tw} and R_{Ta} considering the ability of air and water flow through the bottom surface to be (a) the same (R_B =10 or10000) and (b) different (R_{Bw}=100, R_{Ba}=1 or R_{Bw}=10, R_{Ba}=500).

Figs. 8.10 and 8.11 present the temporal variations of normalized excess PWP and PAP corresponding to three different spatial positions (h/h_s = 0.2, 0.5, and 0.8) of the chosen layer; the normalization is done with respect to the applied load. Unlike Figs. 8.6-8.8, the pore pressure curves in Figs. 8.10 and 8.11 are produced by choosing different *R*-value of the fluid for at least in one of the boundary surfaces. The impact of R_{Ta} (1,5, and 100) and R_{Tw} (1,5, and 100) on the local consolidating curves are described in Figs. 8.10 and 8.11, respectively. The curves are plotted for Darcian and non-Darcian (a=0.2, i_1=45 and θ=0.5) flows. The variation in R_{Ta} influences the consolidating curves of both the fluid phases, whereas, the changes in R_{Tw} solely effects the u_w/q curves but not the u_a/q curves. Moreover, the normalized u_w curves gets affected by R_{Ta} only during the existence of excess PAP; once the excess PAP gets completely dissipated the u_w curves merge together and advances as a unique curve with time. Conversely, R_{Tw} impacts the u_w/q curves after complete dissipation of excess PAP; the impact of the excess PWP curves happen to be earlier for the location adjacent to the top layer. Furthermore, R_{Tw} and R_{Ta} act predominantly on the near-surface zone; therefore, the gap between the u_w-curves generated from the variations in R_{Tw} and R_{Ta} are found to be maximum for h/h_s = 0.2 and minimum for h/h_s = 0.8. Irrespective of the change in *R*-value on the top surface, the influence of flow law occurs earlier and with high impact near the points closer to the top surface of the vadose consolidating zone. The deviation of the Darcian and non-Darcian curves spreads more with the progress in consolidation process.

Fig. 8.12 thoroughly demonstrates the combined impact of R_T and R_B on the consolidation process observed at different point of time, namely, =3.14, 9.14, 15.7, 22.01 and 28.3 ($\times 10^8$ Sec). A series of $U_{avg,w}$ versus R_T curves (for constant R_B) and $U_{avg,w}$ versus R_B curves (for constant R_B) are plotted and joined together to construct the three-

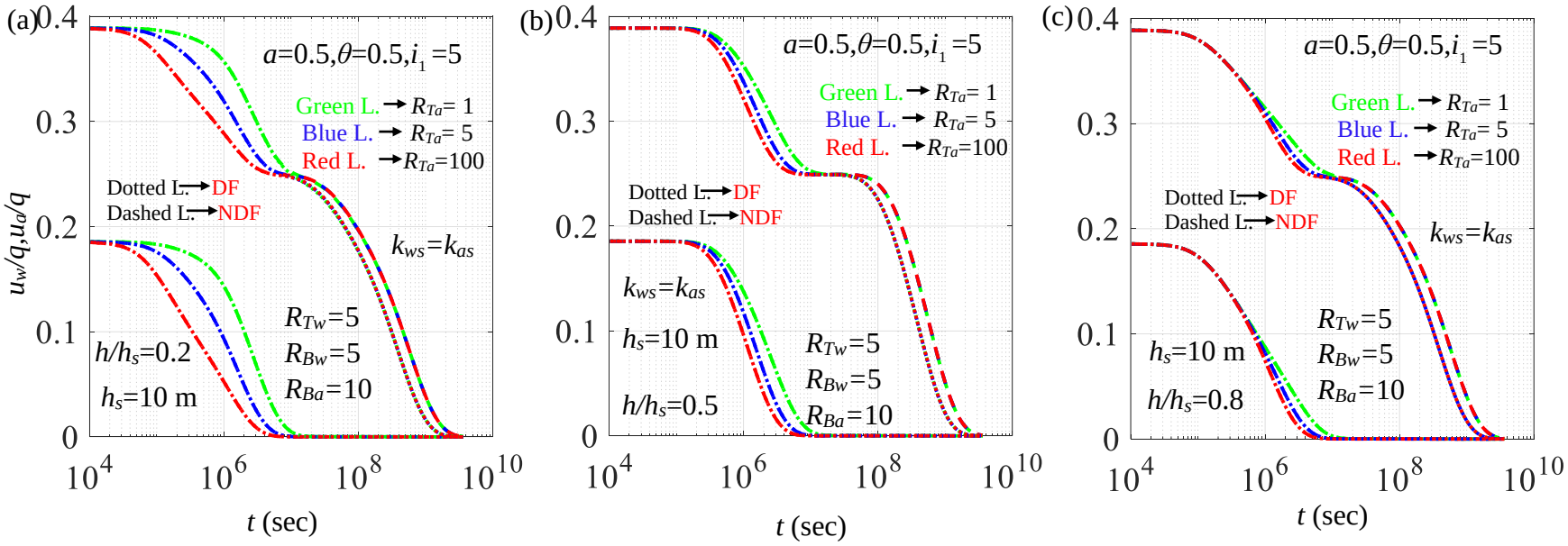

Fig. 8.10 The variation of normalized pore pressures (Darcian and non-Darcian) with time subjected to variable R_{Ta} (=1, 5, and 100) and computed at three different locations (i) h/h_s=0.2, (ii) h/h_s=0.5, and (iii) h/h_s=0.8.

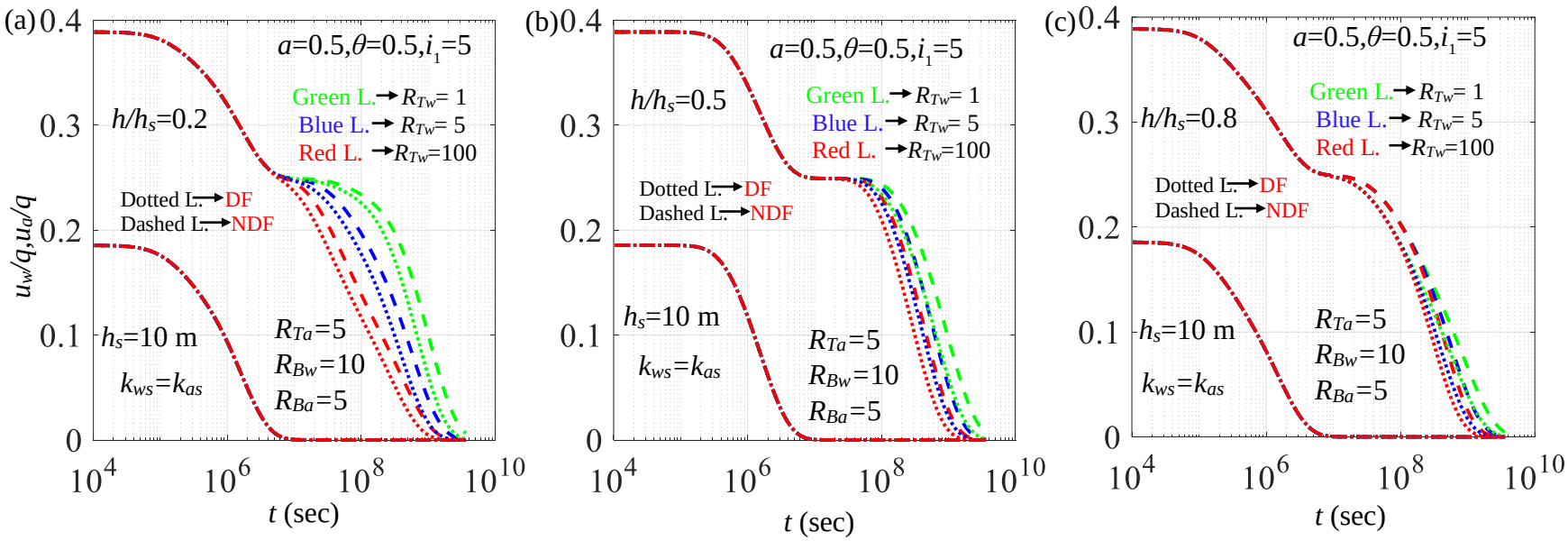

Fig. 8.11 The variation of normalized pore pressures (Darcian and non-Darcian) with time subjected to variable R_{Tw} (=1, 5, and 100) and computed at three different locations (i) h/h_s=0.2, (ii) h/h_s=0.5, and (iii) h/h_s=0.8.

dimensional representative surfaces of $U_{avg,w}$–R_T–R_B. The 3-D surfaces are viewed from two different angles. The average degree of consolidation increases nonlinearly with the increase in R_T and R_B. For a constant time, the magnitude of $U_{avg,w}$ increases sharply upto a certain value of R_T and R_B, and, thereafter, $U_{avg,w}$ remains almost constant. The initial increment rate of $U_{avg,w}$ depends highly on the consolidation time; the higher the consolidation time, the higher the increment rate. After sufficient passage of consolidation time, the variation of $U_{avg,w}$ with R_B (or R_T) at a relatively large R_T (R_B) is quite minimal; however, at relatively smaller consolidation time, the variation of $U_{avg,w}$ with R_B happens to be significant even at a larger R_T.

8.5 VERIFICATION

For understanding the accuracy of the present technique and the reliability of the developed codes, the present numerical solutions are compared with the semi-analytical results reported by Wang et al (2017) and Huang and Zhao (2020) and are presented in Fig. 8.13. Wang et al. (2017) idealized the semi-impermeable impeded drainage boundaries to be symmetric; whereas, Huang and Zhao (2020) considered the asymmetricity of the impeded drainage boundaries. The water flow within the vadose zone obeys the Darcian flow. The verification assessment is carried out on four distinct parameters: (a) normalized isochrones, (b) pore water pressure profile drawn at h/h_s=0.8, (c) temporal variation of $U_{avg,w}$ corresponding to various R_{Tw}, and (d) temporal variation of $U_{avg,a}$ corresponding to various R_{Ta}.

The closeness of the obtained solutions with that of the previously reported analytical solutions provide the confidence on the methodology and the written code. However, there is a minor deviations in the u_w and $U_{avg,w}$ profiles (variation ranges between

0.01% - 5%.), especially in the early stage of consolidation. This can be attributed to the approximations involved in the numerical simulations.

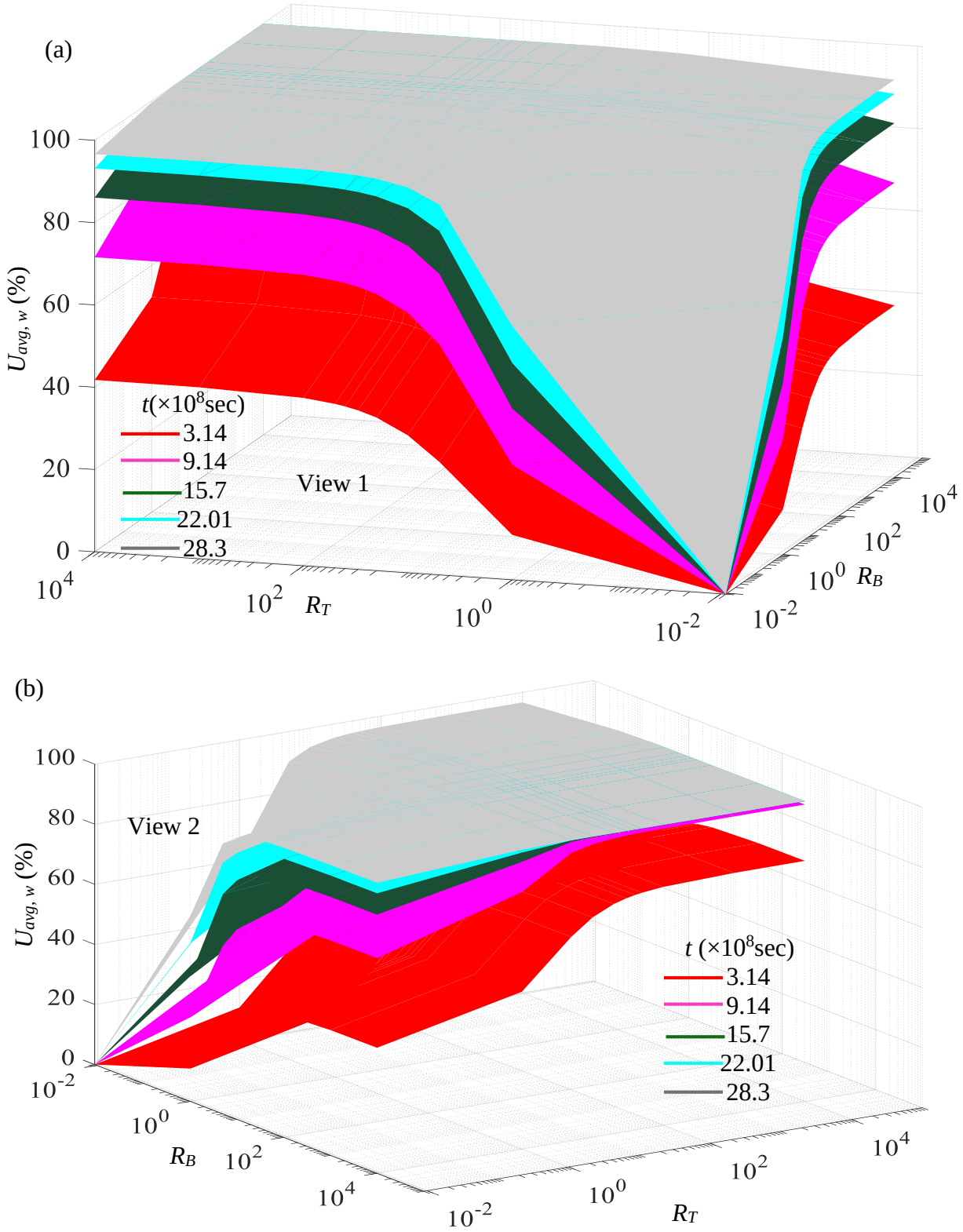

Fig. 8.12 The three-dimensional U_{avg}–R_T–R_B surfaces drawn at different time (a) view 1 (b) view 2.

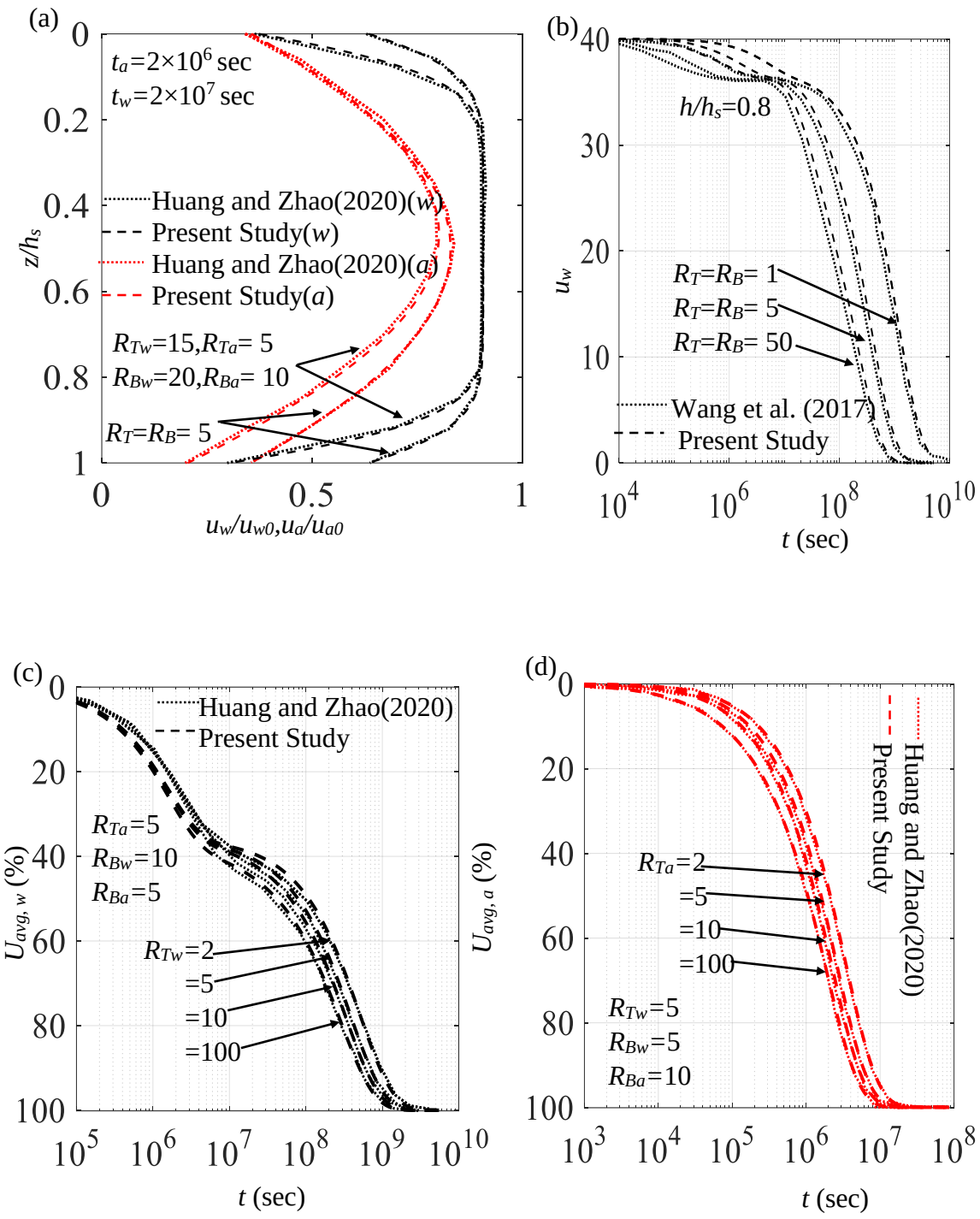

Fig. 8.13 The verifications of the present solutions on the basis of: (a) normalized isochrones, (b) pore water pressure profile drawn at h/h_s=0.8, (c) $U_{avg,w}$ vs. t curves corresponding to various R_{Tw}, and (d) $U_{avg,a}$ vs. t curves corresponding to various R_{Ta}.

8.6 SUMMARY

A thorough numerical investigation is carried out to examine the combined effect of the impeded drainage boundaries and nonlinear fluid flow on the one-dimensional consolidation of unsaturated clays. The impeded drainage boundaries are modelled with the dimensionless semi-permeable parameters and the nonlinear water flow is characterized by the exponent and threshold gradient-based non-Darcian flow. The semi-implicit Crank-Nicolson finite difference technique is used to solve the parabolic partial differential equations representing the diffusion process of the unsaturated consolidating layers. The solutions are reported in terms of the isochrones, pore pressure profiles of certain points, and the time-varying consolidation curves. The figures are plotted by varying the non-Darcian model parameters, permeability ratio of the fluid phases, drain-ability of the fluid phases at top and bottom surfaces. The obtained solutions are critically scrutinized. The influence of the flow law and the drainage boundaries are found to be effective as the consolidation process advances.